

Guided-ion beam measurements of the $O+(4S)+Xe$ charge-transfer reaction

Michael J. Bastian, Rainer A. Dressler, and Edmond Murad

Citation: *The Journal of Chemical Physics* **103**, 144 (1995); doi: 10.1063/1.469652

View online: <http://dx.doi.org/10.1063/1.469652>

View Table of Contents: <http://scitation.aip.org/content/aip/journal/jcp/103/1?ver=pdfcov>

Published by the AIP Publishing

Articles you may be interested in

[Guided-ion beam study of the \$O_2 + C_2H_2\$ charge-transfer and chemical reaction channels](#)

J. Chem. Phys. **110**, 4291 (1999); 10.1063/1.478312

[Charge-transfer reaction of \$14,15N+\(3P_J\)+N_2\(1\Sigma^+g\)\$ from thermal to 100 eV. Crossed-beam and scattering-cell guided-ion beam experiments](#)

J. Chem. Phys. **101**, 3688 (1994); 10.1063/1.467553

[Guided-ion beam measurements of \$X++NO\$ \(\$X=Ar, N_2\$ \) reactions](#)

J. Chem. Phys. **100**, 7348 (1994); 10.1063/1.466879

[Guided-ion beam measurements of \$N++H_2O\$ charge-transfer and chemical reaction channels](#)

J. Chem. Phys. **100**, 5656 (1994); 10.1063/1.467275

[Guided-ion beam studies of the reactions of protonated water clusters, \$H\(H_2O\)_n\$ \(\$n=1-4\$ \), with acetonitrile](#)

J. Chem. Phys. **99**, 1623 (1993); 10.1063/1.465331



NEW Special Topic Sections

NOW ONLINE
Lithium Niobate Properties and Applications:
Reviews of Emerging Trends

AIP Applied Physics Reviews

Guided-ion beam measurements of the $\text{O}^+(^4S)+\text{Xe}$ charge-transfer reaction

Michael J. Bastian,^{a)} Rainer A. Dressler, and Edmond Murad

Phillips Laboratory, Spacecraft Interactions Branch, PL/WSSI, Hanscom AFB, Massachusetts 01731-3010

(Received 17 January 1995; accepted 27 March 1995)

Guided-ion beam integral cross section measurements, product ion time-of-flight (TOF) measurements, and doubly differential cross sections are presented for the $\text{O}^+(^4S)+\text{Xe}\rightarrow\text{O}+\text{Xe}^+$ charge-transfer reaction. The integral cross section is observed to increase monotonically with mean center-of-mass collision energy (E_T) from 0.72 \AA^2 at 0.1 eV to 26.9 \AA^2 at 35.2 eV. Product ion TOF measurements show that the primary contribution to the charge-transfer cross section arises from a direct electron transfer at long range of the Demkov type. The collision energy dependence of the cross section for center-of-mass (c.m.) forward-scattered Xe^+ ions reveals that this minor contribution to the total cross section arises from a hard-sphere-type scattering that primarily involves a Landau–Zener-type diabatic curve crossing at shorter range. Doubly differential cross sections at 4.4 eV indicate that translational to product internal energy transfer is inefficient even at small impact parameters and that the spin-allowed $\text{Xe}^+(^2P)+\text{O}(^3P)$ product channels are preferentially populated. © 1995 American Institute of Physics.

I. INTRODUCTION

In recent years the use of radio-frequency (rf) octopole ion guides^{1,2} has greatly enhanced the ability to determine accurate ion-neutral reaction cross sections in the hyperthermal energy range between near-thermal and ~ 50 eV. The 4π steradian scattered-ion collection of octopole ion guides overcomes the limited collection efficiency problems associated with traditional ion-beam and tandem mass spectrometer methods. The guided-ion beam (GIB) technique has developed at a time where interest is predominantly focused on ion–molecule reactions. Consequently, few good hyperthermal cross section measurements of simple atomic charge-transfer systems exist. The use of a high collection efficiency technique is paramount in the study of light ion–heavy atom collisions, where momentum transfer to the primary ion is efficient.

Ion–atom charge-transfer reactions are fundamental to the understanding of electronically nonadiabatic transitions. The nonadiabatic transition probabilities vary dramatically with collision energy below 10 eV, and the measurement of the charge-transfer cross section energy dependence is, therefore, an excellent test of nonadiabatic transition theories such as the Demkov charge-transfer³ and Landau–Zener-type curve-crossing models.^{4,5}

In this work we present a comprehensive experimental study of the



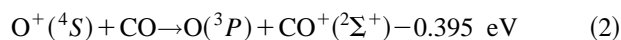
charge-transfer reaction. Despite its simplicity, this atomic charge-transfer system has been the subject of few experimental investigations.⁶ Apart from improving our understanding of charge-transfer dynamics, this work is motivated by the requirement to interpret ionospheric Xe release experiments^{7,8} designed to verify critical ionization velocity (CIV) theory. The concept of CIV postulates^{9–12} that when a neutral gas traverses a weakly magnetized plasma with ki-

netic energy greater than its ionization potential the neutral gas will spontaneously ionize. It is now thought that the injection of the neutral gas into the plasma generates instabilities which energize the ambient electrons. These energized electrons then become the vehicle for ionization. The energy dependence of the absolute cross section for Reaction (1) is required to differentiate between Xe^+ formed via charge-transfer with the major ionospheric ion O^+ , and that produced through CIV.

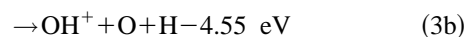
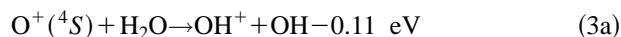
This paper presents absolute integral cross sections, product ion time-of-flight (TOF) measurements, and doubly differential cross sections for Reaction (1). The TOF distributions and doubly differential cross sections provide information on energy partitioning and product ion angular distributions which is used to infer the reaction dynamics and internal energy of the products. The GIB cross sections are approximately eight times larger than previously calculated.⁶ The experimental results are interpreted with respect to the Demkov and Landau–Zener models.

II. EXPERIMENT

The guided-ion beam experiment has been described in detail previously¹³ and only a brief discussion of the experiment will be given here. Oxygen ions are produced in an electron impact source by dissociative ionization of CO_2 with 20.5 eV electrons. This low electron energy avoids formation of the electronically excited $\text{O}^+(^2D)$ and 2P states^{14,15} which lie, respectively, 3.32 and 5.02 eV above the $\text{O}^+(^4S)$ appearance potential of 19.1 eV.^{16,17} The endothermic ionic reactions^{18,19}



and



are used to check for the presence of excited state O^+ . The E_T dependence of the $\text{O}^+ + \text{CO}$ charge-transfer cross section

^{a)}NRC postdoctoral fellow.

indicates that more than 98% of the O^+ ions are in the ground 4S state. The measured absolute values and E_T dependence of the OH^+ integral cross section, for which state-selected measurements have been carried out,¹⁹ also indicate that the source conditions employed essentially produce only $O^+(^4S)$.

The ions produced in the source are accelerated into a Wien filter for mass selection. The emerging ions are decelerated and focused with an injection lens into a system of two octopoles in tandem. The first octopole passes through a 3.5 cm long collision cell which contains Xe at low pressure such that single collision conditions apply, typically 0.028 Pa (0.210 mTorr). A dc-bias potential applied to the octopoles is used to vary the ion-neutral collision energy. The cylindrical effective potential generated by the rf voltage on the octopole rods enables 4π steradian collection of all product Xe^+ ions and unreacted primary O^+ ions. The product and primary ions are extracted from the second octopole with an extraction lens and focused into a quadrupole mass filter. The mass-selected ions are deflected onto a channel electron multiplier. The current pulses from the multiplier are sent into fast amplifier–discriminator electronics and the resulting signal pulses counted by standard means.

For a given collision energy a mass spectrum is obtained which includes both the primary and product ion. In this work the quadrupole mass filter is operated at low ion mass resolution to ensure minimal ion mass discrimination. Low-resolution operation results in flat-top ion mass peak structures in which all isotopes of a given ion mass contribute to a single mass peak. Under these operating conditions²⁰ measurement of the Xe^+ and O^+ mass signal intensities yields the absolute integral cross section. The absolute integral cross section σ in the single collision regime can be determined from

$$\sigma = \frac{I_{\text{prim}}}{(I_{\text{prim}} + I_{\text{prod}})nl}, \quad (4)$$

where I_{prim} is the intensity of the primary ion O^+ , n is the number density of the target neutral Xe, l is the effective length of the primary ion-neutral interaction region, and I_{prod} is the intensity of the product ion Xe^+ . The presence of single collision conditions is established by ensuring that the cross sections determined by Eq. (4) are independent of n . The absence of mass discrimination effects is verified by comparison of the cross sections determined from product ion yields to those derived from primary ion beam attenuation measurements. The absolute accuracy of the integral cross sections are estimated to be $\pm 30\%$. The relative error is substantially smaller.

Retardation scans of the octopole dc-bias potential and calibration of the maximum transverse, or radial, ion energy confined at a given rf octopole voltage are used, respectively, to determine the axial and radial energy distributions of the primary ion beam. The O^+ ion beam lab energy distribution is nearly Gaussian with a FWHM of 0.3 eV. In the TOF mode, comparison of primary ion flight times obtained at several second octopole dc-bias potentials are used to calibrate the mean energy of the primary ion beam to within ± 0.05 eV.

Product and primary ion TOF distributions are obtained by pulsing a deflector electrode in the injection lens to generate 3 to 7 μs wide primary ion beam pulses and recording ion arrival time spectra. After a TOF dwell period the rf voltage on the octopoles is switched off to purge slow ions generated in the previous ion beam pulse from the ion guide. This ensures that each TOF distribution arises from a single ion beam pulse and dramatically lowers the background. The resultant ion TOF distributions are transformed, as described previously,²¹ into ion laboratory axial velocity distributions, $f(v'_{1p})$, where v'_{1p} designates the product ion velocity component parallel to the octopole ion-guide axis.

To further elucidate the charge-transfer dynamics, low-resolution, doubly differential cross sections, $d^2\sigma(v'_{1p}, v'_{1t})/dv'_{1p} dv'_{1t}$, are obtained, where v'_{1t} designates the product ion velocity component transverse, or perpendicular, to the octopole ion-guide axis. The maximum transverse ion energy confinement for a given rf octopole voltage is calibrated as shown by Gerlich.¹ The rf octopole voltage generates an effective confinement potential, V^* , that is systematically lowered to vary the transmission of product ions with respect to v'_{1t} :

$$v'_{1t} < v_0 \equiv \sqrt{\frac{2 eV^*}{M}}, \quad (5)$$

where M is the mass of Xe. The resultant Xe^+ TOF distributions as a function of V^* yield a series of Xe^+ velocity distributions, $f(v'_{1p}, v'_{1t} < v_{0,i})$. These velocity distributions are normalized by the scaling factor C_i :

$$C_i = \frac{\sigma_p(V_i^*)}{\int f(v'_{1p}, v'_{1t} < v_{0,i}) dv'_{1p}}, \quad (6)$$

where $\sigma_p(V_i^*)$ is the measured pulsed cross section for an effective confinement potential V_i^* . The doubly differential cross section $d^2\sigma(v'_{1p}, v'_{1t})/dv'_{1p} dv'_{1t}$ is given by the difference between normalized velocity distributions, $f(v'_{1p}, v'_{1t} < v_{0,i})$, recorded at different V_i^* :

$$\begin{aligned} d^2\sigma(v'_{1p}, v'_{1t})/dv'_{1p} dv'_{1t} \\ = C_1 f(v'_{1p}, v'_{1t} < v_{0,1}) - C_2 f(v'_{1p}, v'_{1t} < v_{0,2}); \end{aligned} \quad (7)$$

$d^2\sigma(v'_{1p}, v'_{1t})/dv'_{1p} dv'_{1t}$ thus represents the flux of product ions scattered into the velocity space volume defined by the cylindrical surfaces of length $v'_{1p} + dv'_{1p}$ and radii $v_{0,1}$ and $v_{0,2}$.

III. RESULTS AND DISCUSSION

A. Semiclassical models

The effective cross section σ_{eff} for a process that involves only two interacting states can be expressed as

$$\sigma_{\text{eff}}(E) = 2\pi \int_0^{b_{\text{max}}} b^2 p(1-p) db, \quad (8)$$

where b is the impact parameter, b_{max} is the maximum impact parameter at which a transition can occur, and p is the impact parameter dependent nonadiabatic transition probability. The Landau–Zener^{4,5,22–25} and Demkov^{3,22,26–28} models are the best-known semiclassical models which de-

scribe the nonadiabatic transition probability in a two-state atomic charge-transfer system. Each model describes one of two distinct cases in which the nonadiabatic coupling exhibits a sharp maximum as a function of the internuclear separation R . In these models, the charge-transfer probability p is related to the diabatic interaction $H_{12} = \langle \Psi_1^d | H | \Psi_2^d \rangle$ between the reactant and product diabatic potential energy surfaces Ψ_1^d and Ψ_2^d , where H is the Hamiltonian of the system. The nonadiabatic transition probability attains a maximum when

$$2H_{12}(R) = \Delta_i(R), \quad (9)$$

where $\Delta_i(R)$ is an energy gap between reactant and product states that is characteristic of the charge-transfer model.

The Landau–Zener model describes a charge-transfer transition localized to the internuclear separation R_c , at which the reactant and product diabatic potential energy curves cross and $\Delta_i(R)$ is the energy gap between *adiabatic* states ΔE_a at the crossing point. The Landau–Zener probability p_{LZ} for a transition from one adiabatic state to another is

$$p_{\text{LZ}} = \exp[-2\pi H_{12}(R_c)^2 / \hbar v_c \Delta F], \quad (10)$$

where ΔF is the difference between the slopes of the diabatic curves at R_c which is traversed at radial velocity v_c .

The Demkov model describes a charge-transfer transition between near resonant reactant and product states where the condition of Eq. (9) is met at a large internuclear separation where the diabatic potential curves are nearly parallel and $\Delta_i(R)$ is the energy gap between *diabatic* curves, ΔE_d . The diabatic interaction at long range can be described by an exponential dependence on the internuclear separation:

$$H_{12}(R) = A e^{-aR}, \quad (11)$$

where A and a are constants, and the Demkov probability p_D for an electron hop between diabatic states is then given by

$$p_D = \frac{1}{1 + \exp[\pi \Delta E_d / \hbar a v_c]}. \quad (12)$$

B. Cross section measurements

Guided-ion beam measurements of the $\text{O}^+(\text{}^4\text{S}) + \text{Xe}$ charge-transfer cross section as a function of mean E_T are presented in Fig. 1. A dramatic increase in the charge-transfer cross section with collision energy is observed. This behavior is typical of other ion–atom systems^{6,15,29–36} where charge-transfer occurs between two near resonant states via a direct mechanism at long range and opposite to that observed in most exothermic ion–molecule systems,^{13,37–40} where long-range attractive ion–neutral forces can dominate the low energy charge-transfer dynamics, resulting in an $(E_T)^{-n}$ dependence. The dramatic difference between the charge-transfer cross section energy dependences of exothermic atomic and molecular systems at collision energies below 1 eV may be attributable to the probability enhancing effects of orbiting collisions in molecular systems. From the present work it may be concluded that orbiting trajectories do not negotiate the Demkov or Landau–Zener transition regions more frequently than direct-scattering events. In molecular systems, on the other hand, it is frequently found that the

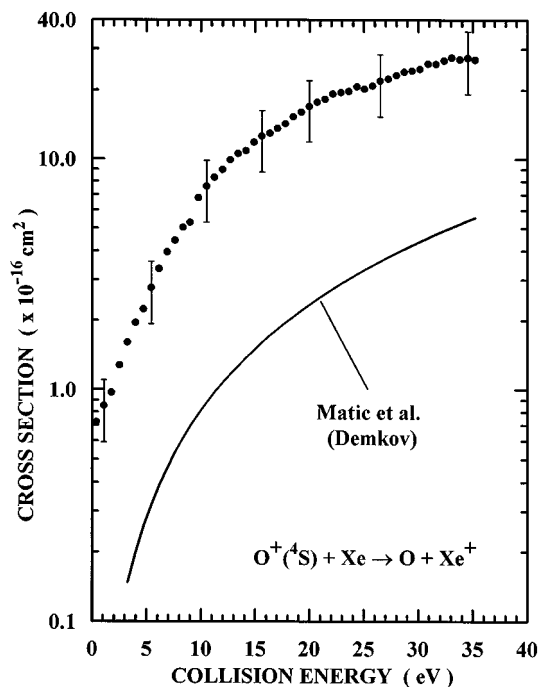


FIG. 1. Integral cross section for the reaction $\text{O}^+(\text{}^4\text{S}) + \text{Xe} \rightarrow \text{O} + \text{Xe}^+$ as a function of E_T . Guided-ion beam cross sections of this work (\bullet) are compared to the theoretical results of Matic *et al.* (—) (Ref. 6). Error bars are $\pm 30\%$.

motion with respect to a vibrational coordinate generates the largest nonadiabatic couplings.⁴¹ Curve crossings thus cover a large range of intermolecular distances and can be passed numerous times during a collision on the vibrational coordinate. Orbiting thus greatly enhances the charge-transfer probability.

The experimental results are compared to the calculated cross sections of Matic *et al.*⁶ which are based on a Demkov-type model of the charge-transfer transition. The experimental and theoretical results exhibit the same qualitative E_T dependence of the cross section but differ significantly in absolute value. Over the E_T range investigated, the experimental cross sections are approximately a factor of 8 greater than the theoretical predictions.

The ground state $\text{XeO}^+(\text{}^4\Sigma^-)$ potential determined from elastic scattering experiments,⁴² and the ion-induced multipole interaction potentials that correlate asymptotically to the reactant $\text{O}^+(\text{}^4\text{S}) + \text{Xe}(\text{}^1\text{S})$ and near resonant product $\text{Xe}^+(\text{}^2P_{1/2}) + \text{O}(\text{}^3\text{P})$ channels are shown in Fig. 2. The potential curves predict a diabatic curve crossing R_c at approximately 3.6 Å which yields a maximum cross section [Eq. (8)] of 20 Å² for a Landau–Zener-type charge-transfer mechanism assuming straight-line trajectories, i.e., $b_{\text{max}} = R_c$. The GIB cross sections exceed 20 Å² at collision energies above 25 eV and continue to increase with energy at 35 eV, the highest collision energy investigated in this study. This implies that charge transfer occurs predominantly at internuclear separations greater than R_c and invokes a Demkov-type mechanism to explain the experimental results.

The quantitative disagreement between present theoretical⁶ and GIB experimental observations may be at-

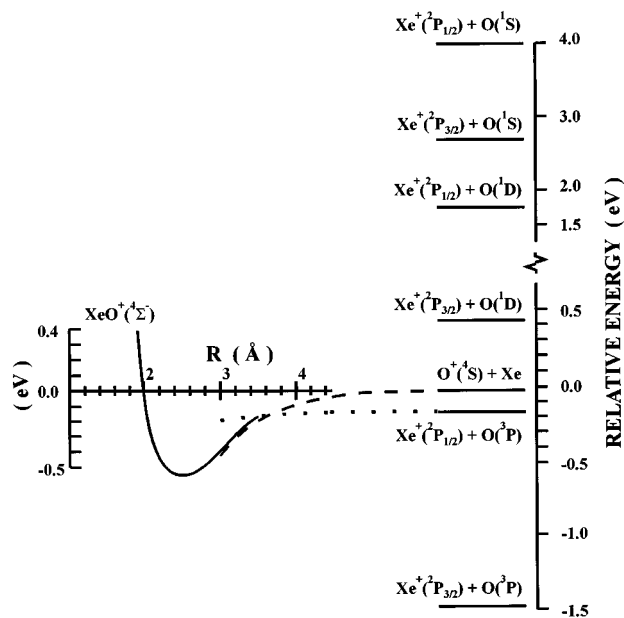


FIG. 2. Energy level diagram for the reaction $O^+(^4S)+Xe \rightarrow O+Xe^+$ and select potentials. Of the product channels shown, only the $O(^3P)+Xe(^2P)$ product channels are allowed for a radial coupling of the diabatic potential energy surfaces, selection rule $\Delta\Lambda=0$, other channels are spin-forbidden. The solid line is the experimentally determined (Ref. 42) ground state $O^+(^4S)+Xe$ potential. The dash and dot lines are the ion-induced multipole interaction potentials which correlate, respectively, to the reactant $O^+(^4S)+Xe$ and product $Xe^+(^2P_{1/2})+O(^3P)$ channels.

tributable to the sensitive dependence of the Demkov charge-transfer probability on the magnitude of the diabatic interaction. Unlike the Landau–Zener model, where H_{12} affects only p_{LZ} [Eq. (10)], the magnitude of H_{12} in the Demkov model affects both the total charge-transfer probability through p_D [Eq. (12)], and the Demkov radius R_D through Eq. (9). Therefore it is conceivable that the calculated diabatic interaction of Matic *et al.*, originally intended to reproduce experimental cross sections⁶ in the E_T range of 1 to 12 keV, underestimates the nonadiabatic coupling and thus the charge-transfer cross section in the collision energy range of this work.

C. Time-of-flight measurements

Typical velocity-transformed TOF distributions $f(v'_{1p})$ are shown in Fig. 3 for several collision energies. The velocity $v_{c.m.}$ marks the center-of-mass (c.m.) velocity and v_{ret} the velocity of product ions that are resonantly forward-scattered. The primary ion beam defines the forward direction and $v_{c.m.}$ and v_{ret} are calculated assuming the target gas is at rest. A large flux of Xe^+ ions with near-zero laboratory-frame velocity is observed at all collision energies. The predominance of these near thermal product ions is consistent with a near resonant, direct, long-range charge-transfer mechanism. Substantial amounts of lab forward-scattered ions are also observed, with particularly high intensity near $v_{c.m.}$. The maxima at $v_{c.m.}$ are attributable to either endothermic product channel population via efficient translational-to-internal energy transfer, i.e., $\Delta E_T \approx -E_T$, and/or large angu-

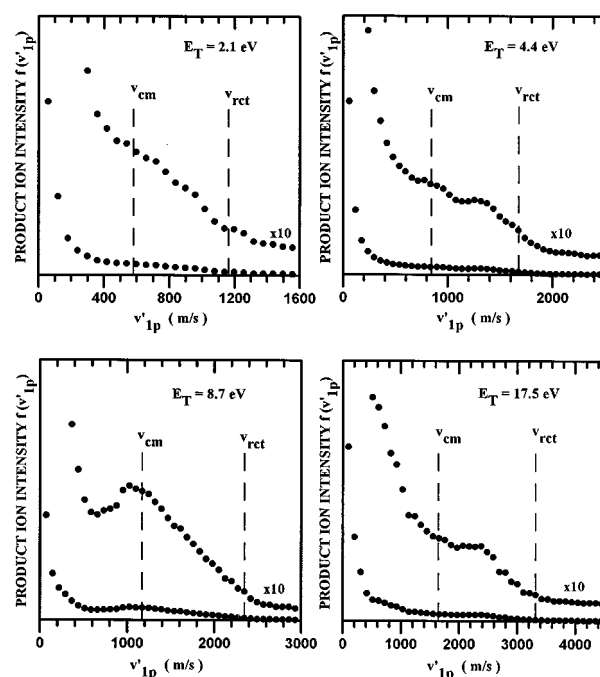


FIG. 3. Velocity-transformed TOF distributions $f(v'_{1p})$ of the Xe^+ product ion at several collision energies. The product ion velocities $v_{c.m.}$ and v_{ret} mark, respectively, the c.m. velocity and the velocity for resonantly forward-scattered product ions assuming a target gas at rest.

lar scattering. An energy level diagram of possible product states accessed by the reactants is shown in Fig. 2.

D. Low-resolution angular scattering distribution

To explore in greater detail the energy partitioning and dynamics of Reaction (1), TOF measurements at five octopole confinement potentials, V^* , recorded at $E_T=4.4$ eV are used to construct the product ion angular scattering distribution shown in Fig. 4. The contours connect points of equal $d^2\sigma(v'_{1p}, v'_{1t})/dv'_{1p} dv'_{1t}$. The dashed arcs labeled

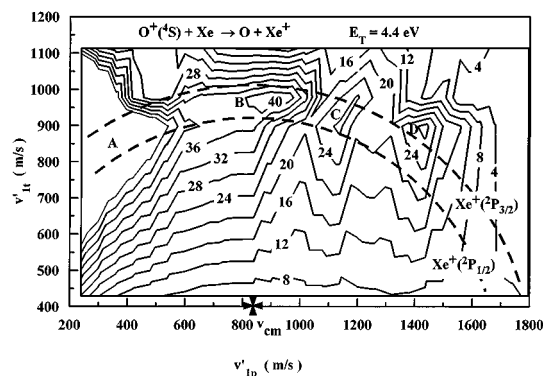


FIG. 4. Product ion angular scattering distribution for $E_T=4.4$ eV, derived from five $f(v'_{1p}, v'_{1t} < v_{0,i})$. The results are presented as a contour plot where contours connect points of equal $d^2\sigma(v'_{1p}, v'_{1t})/dv'_{1p} dv'_{1t}$. The cross indicates the c.m. velocity and the dashed arcs are loci of constant translational exoergicity ΔE_T for the product channels $O(^3P)+Xe(^2P_{1/2})$ and $O(^3P)+Xe(^2P_{3/2})$. The bands labeled A, B, C, and D mark maxima in the scattered Xe^+ flux. For clarity, the contour values have been scaled by $\times 1000$ and scaled values above 48 have been omitted.

$Xe^+(^2P_{1/2})$ and $Xe^+(^2P_{3/2})$ are loci of constant translational exoergicity ΔE_T for the respective $O(^3P)+Xe^+(^2P_{1/2})$ and $O(^3P)+Xe^+(^2P_{3/2})$ product channels. Maxima observed in the scattered Xe^+ flux, labeled bands A, B, C, and D, all essentially appear at the translational exoergicity of the spin-allowed $O(^3P)+Xe^+(^2P)$ product channels. The slight displacement of band D outside the $Xe^+(^2P_{3/2})$ exoergicity limit is within the combined uncertainty of the TOF measurements and V^* calibration. The contours of the most intense maximum, band A, are not shown above 48 for the sake of clarity. Band A exhibits significant intensity beyond the product ground electronic state locus. This signal is an experimental artifact attributable to surface-potential barriers that obstruct very slow ions as the confinement potential, V^* , is lowered and the respective ion trajectories come closer to the octopole rods. Despite the low v'_{1t} of these ions, a change in their transmission is registered at confinement potentials associated with relatively high v'_{1t} . Band A, however, clearly exhibits a “ridge” of Xe^+ flux which extends in the direction of the $O(^3P)+Xe^+(^2P_{1/2})$ translational exoergicity locus, implying a preference for population of the nearest resonant product channel.

The absence of any maxima in the Xe^+ flux for a translational exoergicity less than that of the $O(^3P)+Xe^+(^2P_{1/2})$ product channel indicates that the charge-transfer reaction exhibits no noticeable translational-to-internal energy transfer, i.e., endothermic product channel population. This is consistent with the selection rules for a nonadiabatic transition induced by radial coupling of the adiabatic surfaces, $\Delta\Lambda=0$, $\pm\leftrightarrow\pm$, $g(u)\leftrightarrow g(u)$, and implies that nonadiabatic transitions do not occur on the repulsive wall. Therefore, the high flux at $v_{c.m.}$ in the velocity-transformed TOF spectra at $E_T=4.4$ eV (Fig. 3) is primarily due to 90° scattering in the c.m. frame of near resonant products and not due to efficient conversion of translational energy into internal modes ($\Delta E_T \approx -E_T$).

E. Forward-scattered cross sections

The fraction of product ion signal with $v'_{1p} > v_{c.m.}$ multiplied by the cross section obtained in the pulsed TOF mode yields the forward-scattered cross section $\sigma(v'_{1p} > v_{c.m.})$ shown in Fig. 5 as a function of collision energy. In previous investigations of molecular charge-transfer systems,^{13,39,40} an observed $(E_T)^{-n}$ dependence of $\sigma(v'_{1p} > v_{c.m.})$ was regarded as evidence that forward-scattered ions are attributable to orbiting collisions mediated by the long-range attractive forces of the ion-neutral interaction. The marked increase in $\sigma(v'_{1p} > v_{c.m.})$ with E_T observed for Reaction (1) clearly suggests that forward-scattered Xe^+ ions are produced in smaller impact parameter collisions where the repulsive wall of the ion-neutral interaction is sampled.

The potential curves (Fig. 2) predict a $XeO^+(^4\Sigma^-)$ potential surface⁴² zero crossing at approximately 2.0 Å, therefore ions which encounter the repulsive region of the ion-neutral interaction must negotiate the diabatic curve crossing at approximately 3.6 Å. Since the angular scattering distribution in Fig. 4 demonstrates that forward-scattered products are primarily formed in the nearest resonant state, it is rea-

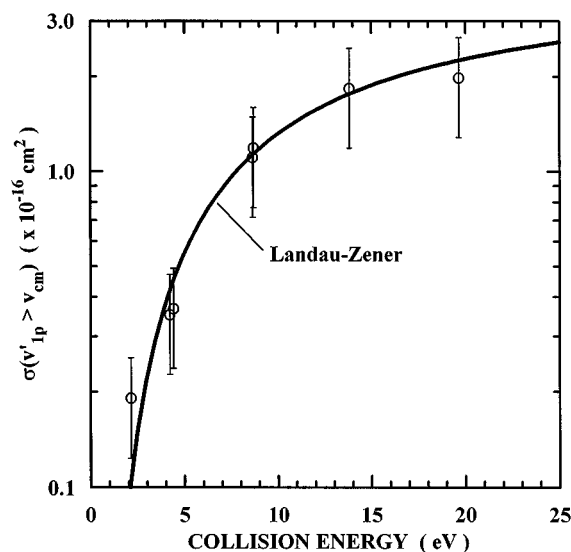


FIG. 5. Center-of-mass forward-scattered cross section $\sigma(v'_{1p} > v_{c.m.})$ for the charge-transfer reaction $O^+(^4S)+Xe \rightarrow O+Xe^+$ as a function of E_T . The Xe^+ c.m. forward-scattered cross sections (\circ) of this work are compared to the best fit of a Landau-Zener model (—) to the forward-scattered cross section E_T dependence. The parameters of the fit are $b_{\max}=1.5\pm0.2$ Å, $H_{12}=0.07\pm0.02$ eV, and $R_c=3.6$ Å. The fit is discussed in Sec. III E. Error bars are $\pm 40\%$.

sonable to assume that the nonadiabatic transitions in forward-scattered trajectories predominantly occur at the respective crossing. We find that the E_T dependence of the forward-scattered cross section is well represented by a Landau-Zener model of the charge-transfer transition in which only the near resonant $O(^3P)+Xe^+(^2P_{1/2})$ product channel is populated. The values of b_{\max} and H_{12} in, respectively, Eqs. (8) and (10), are varied while maintaining $R_c=3.6$ Å and properly determining the impact parameter dependent radial velocity $v_c=\dot{R}(R_c,b)$ for a straight-line trajectory. The values $b_{\max}=1.5\pm0.2$ Å and $H_{12}=0.07\pm0.02$ eV yield a best fit, which is compared to the experimental results in Fig. 5. The determined b_{\max} corresponds to the hard-sphere radius for a straight-line trajectory and is smaller than the $XeO^+(^4\Sigma^-)$ potential surface⁴¹ zero crossing. The applied model is thus consistent with the potential and corroborates the angular scattering measurements.

IV. CONCLUSIONS

The energy dependence of the $O^+(^4S)+Xe \rightarrow O+Xe^+$ integral charge-transfer cross section and product ion velocity distributions reveal that the charge-transfer dynamics are dominated by a nonadiabatic transition at long-range, of the Demkov-type, in which little momentum transfer occurs. The present quantitative disagreement between theoretical⁶ and GIB $O^+(^4S)+Xe$ charge-transfer cross sections is attributed to the sensitive dependence of the long-range Demkov charge-transfer probability on the calculated diabatic interaction. Approximately 10% to 20% of the integral cross section is associated with smaller impact parameter trajectories that involve a Landau-Zener-type charge-transfer mechanism.

The substantially larger GIB cross sections have important implications for both the current feasibility and past interpretation of ionospheric CIV experiments. Ionospheric experimenters have used estimates of 4.8 \AA^2 at $E_T=5 \text{ eV}$,^{8,43} and 1 \AA^2 at $E_T=10 \text{ eV}$,⁴⁴ the latter based on the calculations of Matic *et al.*,⁶ for the charge-transfer cross section. The experimental measurements presented in this work indicate that the integral charge-transfer cross section for Reaction (1) at 5 eV is $2.4 \pm 0.5 \text{ \AA}^2$ and is $7.0 \pm 2 \text{ \AA}^2$ at 10 eV.

ACKNOWLEDGMENTS

This work was supported by AFOSR under Task No. 2303EP2 and was performed while the author M.J.B. held a National Research Council–Phillips Laboratory Research Associateship. The authors are grateful to C. Y. Ng and co-workers for communicating the results of their $O^+(^4S)+H_2O$ studies prior to publication.

¹D. Gerlich, in *State-Selected and State-to-State Ion–Molecule Reaction Dynamics, Part I. Experiment*, edited by M. Baer and C. Y. Ng (Wiley, New York, 1992), pp. 1–176.

²C. Y. Ng, in *State-Selected and State-to-State Ion–Molecule Reaction Dynamics, Part I. Experiment*, edited by M. Baer and C. Y. Ng (Wiley, New York, 1992), pp. 401–500.

³Yu. N. Demkov, JETP **18**, 138 (1964).

⁴C. Zener, Proc. R. Soc. London Ser. A **137**, 696 (1932).

⁵L. D. Landau, Phys. Z. Sowjetunion **2**, 46 (1932).

⁶M. Matic, V. Sidis, M. Vujovic, and B. Cobic, J. Phys. B **13**, 3665 (1980).

⁷J. A. Marshall, J. L. Burch, E. Y. Choueiri, and N. Kawashima, Geophys. Res. Lett. **20**, 499 (1993).

⁸S. T. Lai, E. Murad, C. P. Pike, W. J. McNeil, and A. Setayesh, Adv. Space Res. **13**, 81 (1993).

⁹S. T. Lai and E. Murad, IEEE Trans. Plasma Sci. **20**, 770 (1992).

¹⁰C. K. Goertz, S. Machida, and G. Lu, Adv. Space Res. **10**, 33 (1990).

¹¹H. Alfvén, Rev. Mod. Phys. **32**, 710 (1960).

¹²H. Alfvén, *On the Origin of the Solar System* (Oxford University, Oxford, 1954).

¹³R. A. Dressler, R. H. Salter, and E. Murad, J. Chem. Phys. **99**, 1159 (1993).

¹⁴C. E. Moore, Natl. Bur. Stand. Circ. **467** (1969).

¹⁵B. M. Hughes and T. O. Tiernan, J. Chem. Phys. **55**, 3419 (1971).

¹⁶J. A. Appell, J. Durup, and F. Heitz, Adv. Mass Spectrom. **3**, 457 (1969).

¹⁷J. L. Franklin, J. G. Dillard, H. M. Rosenstock, J. T. Herron, and K. Draxl, Natl. Stand. Ref. Data Ser. **26** (1969).

¹⁸E. Murad, J. Chem. Phys. **58**, 4374 (1973).

¹⁹X.-Li, Y.-L. Huang, G. D. Flesch, and C. Y. Ng, J. Chem. Phys. **102**, 5100 (1995).

²⁰G. D. Flesch, S. Nourbakhsh, and C. Y. Ng, J. Chem. Phys. **92**, 3590 (1990).

²¹R. A. Dressler, R. H. Salter, and E. Murad, Chem. Phys. Lett. **204**, 111 (1993).

²²*State-Selected and State-to-State Ion–Molecule Reaction Dynamics, Part 2. Theory*, edited by M. Baer and C. Y. Ng (Wiley, New York, 1992).

²³R. D. Levine and R. B. Bernstein, *Molecular Reaction Dynamics and Chemical Reactivity* (Oxford University, New York, 1987).

²⁴M. S. Child, *Molecular Collisions* (Academic, New York, 1974).

²⁵R. E. Olson, F. T. Smith, and E. Bauer, Appl. Opt. **10**, 1848 (1971).

²⁶P. Archirel and B. Levy, Chem. Phys. **106**, 51 (1986).

²⁷T. R. Dinterman and J. B. Delos, Phys. Rev. A **15**, 463 (1977).

²⁸D. Rapp and E. W. Francis, J. Chem. Phys. **37**, 2631 (1962).

²⁹T. F. Moran and J. B. Wilcox, J. Chem. Phys. **70**, 1467 (1979).

³⁰T. F. Moran and J. B. Wilcox, J. Chem. Phys. **69**, 1397 (1978).

³¹M. Vujovic, M. Matic, B. Cobic, and P. Hvelplund, J. Phys. B **10**, 3699 (1977).

³²J. A. Rutherford and D. A. Vroom, J. Chem. Phys. **65**, 1603 (1976).

³³J. A. Rutherford and D. A. Vroom, J. Chem. Phys. **62**, 1460 (1975).

³⁴J. H. Ormrod and W. L. Michel, Can. J. Phys. **49**, 606 (1971).

³⁵J. R. Peterson and D. C. Lorents, Phys. Rev. **182**, 152 (1969).

³⁶J. Perel, R. H. Vernon, and H. L. Daley, Phys. Rev. **138**, 937 (1965).

³⁷S. T. Arnold, R. A. Dressler, M. J. Bastian, J. A. Gardner, and E. Murad, J. Chem. Phys. (submitted).

³⁸R. A. Dressler and E. Murad, in *Unimolecular and Bimolecular Reaction Dynamics*, edited by C. Y. Ng, T. Baer, and I. Powis (Wiley, New York, 1994), pp. 87–182.

³⁹R. A. Dressler and E. Murad, J. Chem. Phys. **100**, 5656 (1994).

⁴⁰S. T. Graul, S. Williams, R. A. Dressler, R. H. Salter, and E. Murad, J. Chem. Phys. **100**, 7348 (1994).

⁴¹K. Yamashita, K. Morokuma, Y. Shiraishi, and I. Kusunoski, J. Chem. Phys. **92**, 2505 (1990).

⁴²M. F. Guest, A. Ding, J. Karlau, J. Weise, and I. H. Hiller, Mol. Phys. **38**, 1427 (1979).

⁴³I. Axnäs, Geophys. Res. Lett. **7**, 933 (1980).

⁴⁴H. Okuda and E. Y. Choueiri, Phys. Plasma **1**, 1669 (1993).